Joule

CellPress

Article

A Dynamic, Electrolyte-Blocking, and Single-Ion-Conductive Network for Stable Lithium-Metal Anodes

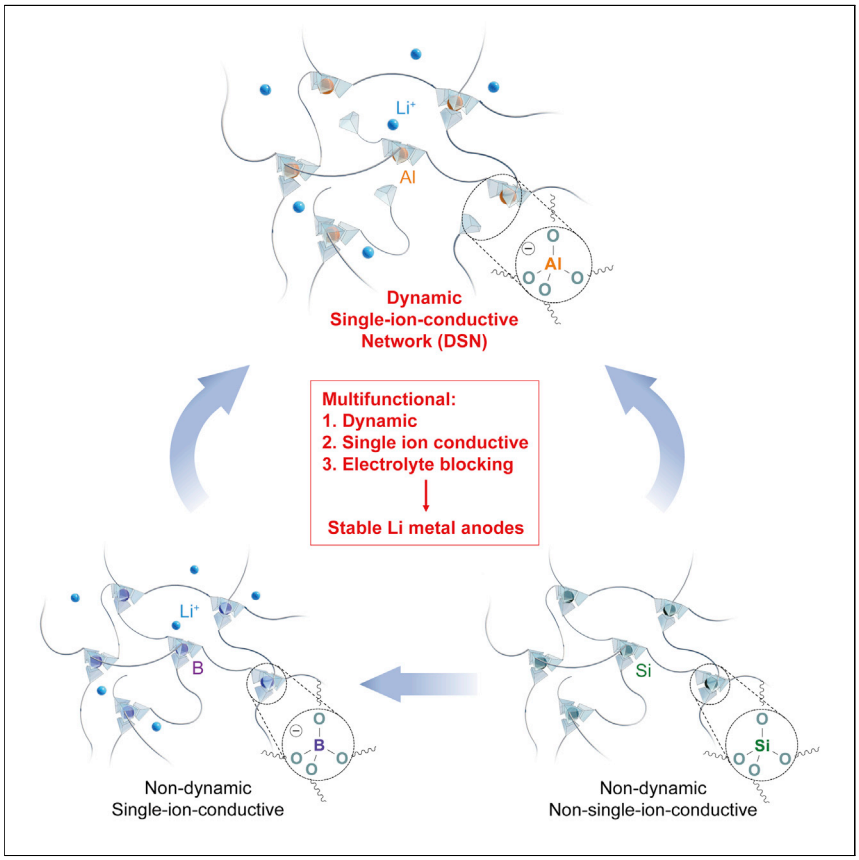

In this work, we designed a multifunctional material to improve the stability of lithium-metal anodes. By integrating dynamic flowability, fast single-ion conduction, and electrolyte-blocking property into a single matrix, the dynamic single-ion-conductive network (DSN), we achieved long cycle life for lithium-metal full batteries in commercial carbonate electrolyte. The solution processability of DSN is promising for its application in practical lithium-metal batteries. We also systematically tuned the crosslinking chemistry to study the synergistic stabilizing effects.

Zhiao Yu, David G. Mackanic, Wesley Michaels, ..., Jian Qin, Yi Cui, Zhenan Bao

yicui@stanford.edu (Y.C.)
zbao@stanford.edu (Z.B.)

HIGHLIGHTS

A multifunctional network material is proposed to stabilize lithium-metal anodes

Improved cyclability is achieved for high-voltage lithium-metal full battery

Direct lithium-metal processability enables practical application

Crosslinking chemistry is tuned to study the synergistic stabilizing effects

Yu et al., Joule 3, 1–16
November 20, 2019
https://doi.org/10.1016/j.joule.2019.07.025

Please cite this article in press as: Yu et al., A Dynamic, Electrolyte-Blocking, and Single-Ion-Conductive Network for Stable Lithium-Metal Anodes, Joule (2019), https://doi.org/10.1016/j.joule.2019.07.025

Joule

CellPress

Article

A Dynamic, Electrolyte-Blocking, and Single-Ion-Conductive Network for Stable Lithium-Metal Anodes

Zhiao Yu,[1,2,8] David G. Mackanic,[1,8] Wesley Michaels,[1] Minah Lee,[1,3] Allen Pei,[4] Dawei Feng,[1] Qiuhong Zhang,[1,5] Yuchi Tsao,[1,2] Chibueze V. Amanchukwu,[1] Xuzhou Yan,[1,6] Hansen Wang,[4] Shucheng Chen,[1] Kai Liu,[4] Jiheong Kang,[1] Jian Qin,[1] Yi Cui,[4,7,*] and Zhenan Bao[1,9,*]

SUMMARY

Implementation of lithium (Li)-metal anodes requires developments to solve the heterogeneity and instability issues of naturally formed solid-electrolyte interphase (SEI). The artificial SEI, as an alternative, enables an ideal interface by regulating critical features such as fast ion transport, conformal protection, and parasitic reaction mitigation. Herein, for the first time, we integrate all of these desired properties into a single matrix, the dynamic single-ion-conductive network (DSN), as a multifunctional artificial SEI. The DSN incorporates the tetrahedral $Al(OR)_4^-$ (R = soft fluorinated linker) centers as both dynamic bonding motifs and counter anions, endowing it with flowability and Li^+ single-ion conductivity. Simultaneously, the fluorinated linkers provide chain mobility and electrolyte-blocking capability. A solution-processed DSN coating was found to simultaneously hinder electrolyte penetration, mitigate side reactions between Li and electrolyte, maintain low interfacial impedance, and allow homogenous Li deposition. With this coating, long cycle life and high Coulombic efficiency are achieved for Li-metal battery in a commercial carbonate electrolyte.

INTRODUCTION

Recent years have witnessed an exponential growth in demand for high-density energy storage devices, in which the lithium (Li)-ion battery plays an increasingly significant role.[1–5] However, conventional Li-ion batteries are nearing their theoretical capacity limit.[2,3] Therefore, it is crucial to develop a new generation of batteries to fulfill the aggressive energy density requirements of modern mobile phones, portable computers, electrical vehicles, and other electronic devices.[5–8] Li metal is an ideal candidate because it has both high theoretical specific capacity (3,860 mAh g^{-1}) and low electrochemical potential (−3.04 V versus standard hydrogen electrode) of any known negative electrode material.[2,7,9,10] It has the potential to provide the highest specific energy as an anode for the Li battery.[6,7]

Despite its promises, Li-metal anode is challenging to implement due to several drawbacks.[6,7,11,12] First, Li easily reacts with electrolytes to form a solid-electrolyte interphase (SEI).[13–17] The typically heterogeneous nature of the SEI results in local fluctuation of Li^+ ion flux and current density, which lead to the formation of dendrites.[18] Second, large volume change during Li stripping and plating creates cracks in the brittle SEI, forms dead Li, and causes further electrolyte consumption.[18,19] The above effects lower the Coulombic efficiency (CE) and devastate the cycle life of Li-metal anodes.[6,20,21] To mitigate the aforementioned degradation pathways,

Context & Scale

Lithium (Li)-metal batteries are attractive due to their high energy density. However, the drastic reactivity of Li metal limits its battery performance due to the formation of a naturally heterogeneous solid-electrolyte interphase (SEI) on the surface. To solve this issue, a rationally designed artificial SEI is utilized to replace the natural SEI. All the ideal properties for an artificial SEI are integrated into one matrix, such as conformal protection, fast Li^+ single-ion transport, and harmful parasitic reaction mitigation. The resulting material, a dynamic single-ion-conductive network, is found to greatly improve Li-metal performance in commercial carbonate electrolyte. High-performance full cell batteries are achieved using solution-processed Li-metal anodes. Furthermore, a systematic study of the synergistic effects on stabilizing Li metal is conducted. Therefore, this work provides a detailed strategy for designing artificial SEI and enabling high performance in a Li-metal battery.

Please cite this article in press as: Yu et al., A Dynamic, Electrolyte-Blocking, and Single-Ion-Conductive Network for Stable Lithium-Metal Anodes, Joule (2019), https://doi.org/10.1016/j.joule.2019.07.025

strategies pursued include modifying components of the liquid electrolyte,[13,22–24] introducing electrolyte additives,[25–28] utilizing solid electrolytes,[17,29–33] employing a shielding cation layer,[34] or chemically pretreating Li metal.[35,36] Nevertheless, it remains challenging to achieve a stable SEI on Li metal;[6,15] therefore, the artificial SEI[14,18,19,37–42] is particularly promising as an alternative strategy to replace the native SEI on Li.

An ideal artificial SEI must have several key properties. First, previous work proposed benefits of having high modulus coatings on Li;[15,17] however, our recent work suggested flowability and dynamic property allow SEI to adapt to large volume change during Li stripping and plating, and result in uniform Li deposition macroscopically.[18,38,43] Second, uniform and fast Li^+ single-ion conduction in the artificial SEI is found to be beneficial to reduce "hot spots", increase critical Li deposit size, and stabilize the Li-metal anode.[14,17,44,45] Finally, the SEI needs to be both chemically and electrochemically inert itself and mitigate electrolyte penetration to minimize deleterious side reactions between Li and coating or Li and electrolyte.[14] Nevertheless, few artificial SEIs possess all the desirable properties such as dynamic property,[18] flowability,[38] or high ion conductivity.[35,37,44] Additionally, the majority of the reported Li-metal artificial SEIs are only compatible with ether-based electrolytes (Table S1 and its Plot), making them incompatible with high-voltage, high-energy-density lithium nickel manganese cobalt oxide (NMC) cathodes that are used in today's commercial Li-ion batteries. Herein, we report an artificial SEI design based on a dynamic polymeric network with high Li^+ single-ion conductivity. In this network, tetrahedral $Al(OR)_4^-$ (R = soft fluorinated linker) anions are used for the first time as a dynamic motif while providing counter anions for Li^+ ions (Figure 1A). With this dynamic single-ion-conductive network (DSN) as an artificial SEI, we demonstrate over 400 stable stripping and plating cycles in Li||Cu cell using commercial carbonate-based electrolyte. Greater than 85% capacity retention for over 160 cycles in a Li||NMC full battery was achieved using directly coated thin Li foils and commercial, industry-standard NMC cathode sheets. The design concept of using dynamic single-ion conductor as a stable and scalable artificial SEI is promising for practical Li-metal batteries.

RESULTS AND DISCUSSION

Material Design

To prepare the DSN, tetrahedral $Al(OR)_4^-$ anions were used as dynamic crosslinking centers. Previous work reported the reversibility of the Al-O bond,[46,47] yet it has never been employed as a source of dynamic flowability. The Li^+ counter ions are introduced as the mobile ions in the network, while soft fluorinated chains (1H,1H,11H,11H-perfluoro-3,6,9-trioxaundecane-1,11-diol, FTEG) are chosen as inert ligands (Figure 1A). The FTEG is less chemically reactive and more solvent resistant compared to its non-fluorinated version, poly(ethylene oxide) (PEO)[43,48,49] and therefore can potentially mitigate side reactions between Li and DSN, prevent the dissolution of DSN in the polar carbonate electrolyte, and reduce the penetration of the electrolyte through DSN. Furthermore, the flexible FTEG chains ensure flowability when combined with dynamic $Al(OR)_4^-$ crosslinking sites. Since Li^+ ions are directly introduced during the synthesis of DSN, it can transport through the network of fixed $Al(OR)_4^-$ anions, making DSN a solid-state single-ion conductor.

To confirm the effects of single-ion conductivity and dynamic property on the performance of artificial SEI materials, we designed two additional networks, in which the Al centers were substituted with the single-ion-conductive yet non-dynamic

[1]Department of Chemical Engineering, Stanford University, Stanford, CA, USA

[2]Department of Chemistry, Stanford University, Stanford, CA 94305, USA

[3]Center for Energy Storage Research, Korea Institute of Science and Technology (KIST), Seoul 02792, Republic of Korea

[4]Department of Materials Science and Engineering, Stanford University, Stanford, CA 94305, USA

[5]Department of Polymer Science and Engineering, Nanjing University, Nanjing 210093, China

[6]School of Chemistry and Chemical Engineering, Shanghai Jiao Tong University, Shanghai 200240, China

[7]SLAC National Accelerator Laboratory, Stanford Institute for Materials and Energy Sciences, Menlo Park, CA 94025, USA

[8]These authors contributed equally

[9]Lead Contact

*Correspondence: yicui@stanford.edu (Y.C.), zbao@stanford.edu (Z.B.)

https://doi.org/10.1016/j.joule.2019.07.025

Please cite this article in press as: Yu et al., A Dynamic, Electrolyte-Blocking, and Single-Ion-Conductive Network for Stable Lithium-Metal Anodes, Joule (2019), https://doi.org/10.1016/j.joule.2019.07.025

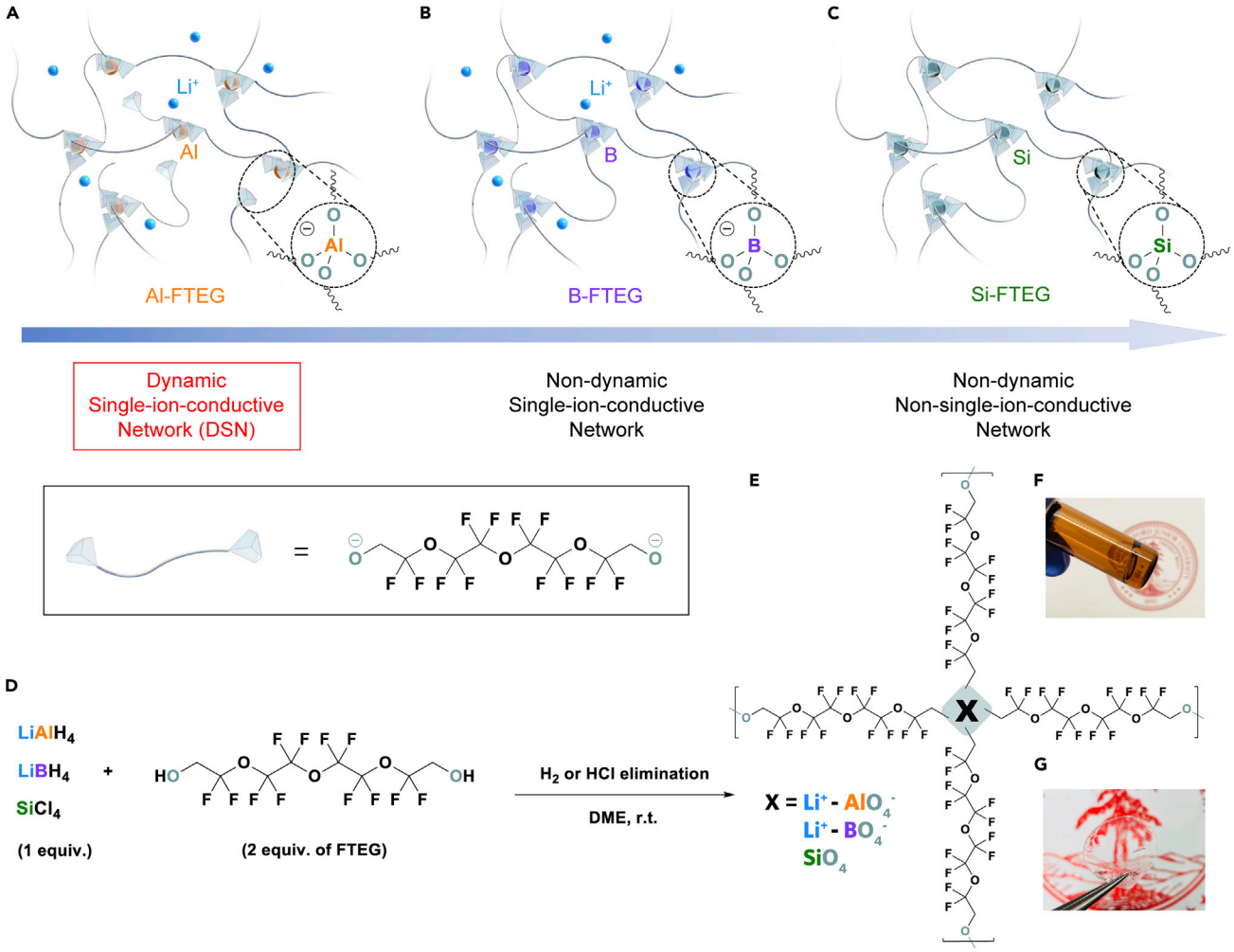

Figure 1. Material Design and Chemical Structures of DSN and Derivatives

(A–C) Conceptual sketch of Al-FTEG (DSN) (A), B-FTEG (B), and Si-FTEG (C). Blue spheres, Li^+ ions; orange spheres, Al atoms; purple spheres, B atoms; olive spheres, Si atoms; tetrahedra, anion centers; gray chains, soft ligands.

(D) The reaction to synthesize DSN derivatives.

(E) Detailed chemical structure of DSN derivatives.

(F and G) Photo of an as-synthesized viscous DSN/DME solution (F) and a free-standing DSN film (G).

B centers (B-FTEG) or the neither single-ion-conductive nor dynamic Si centers (Si-FTEG), respectively (Figures 1B, 1C, S1, and S2). These designs allow for the fine tuning of electrochemical and mechanical properties of the artificial SEIs and provide a platform to understand their structure-property relationships. The chemical characterizations and costs of the prepared materials are provided in Figures 1D and S3–S5 and Table S2.

Mechanical Property

Viscoelasticity and dynamic properties have previously been identified as properties that improve Li deposition in artificial SEI materials.[18,38] The rheology measurement of bulk DSN material clearly shows its viscoelasticity (Figure 2A and Videos S1 and S2). At frequencies higher than 45 Hz, the storage modulus becomes greater than the loss modulus ($G' > G''$), which yields a short relaxation time of ~0.022 s (Figure S6). Such a liquid-like behavior at low frequency will potentially allow DSN to

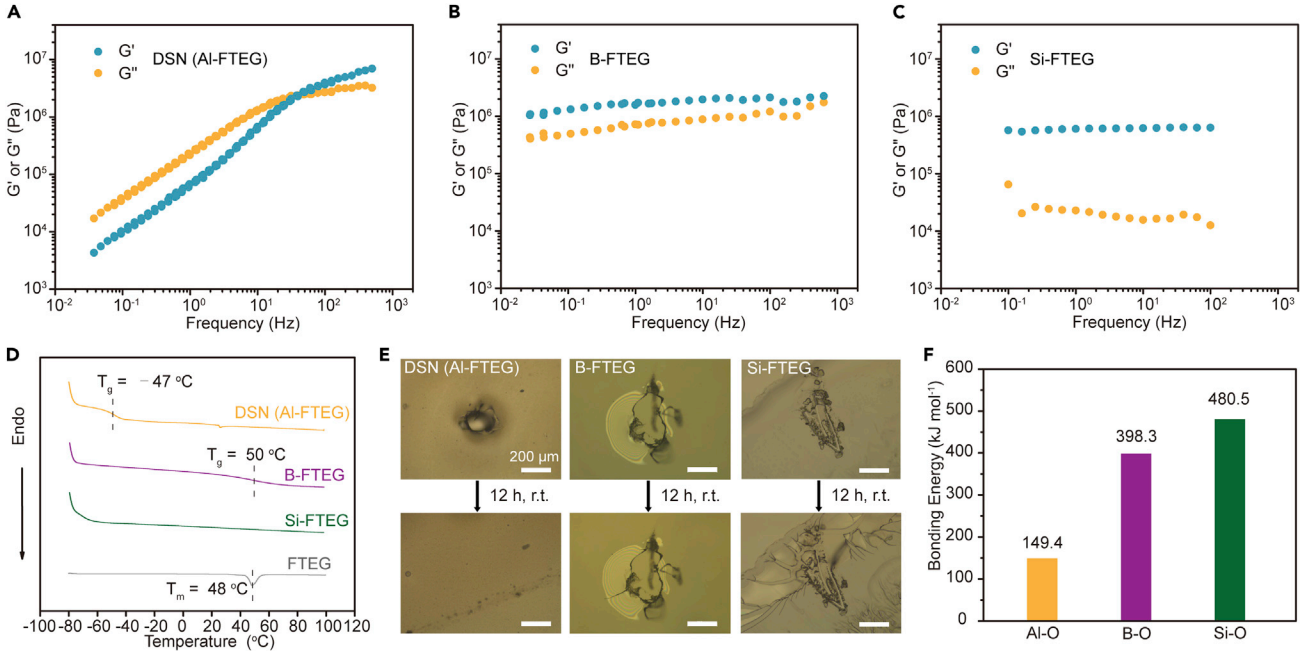

Figure 2. Mechanical Property of DSN and the Dynamic Nature of $Al(OR)_4^-$ Coordination Bond

(A–C) Rheology measurements of DSN (A), B-FTEG (B), and Si-FTEG (C).

(D) DSC of DSN derivatives and FTEG.

(E) Optical microscope pictures for dynamic property test. Scale bars, 200 μm.

(F) Comparison of Al-O, B-O, and Si-O bonding energies calculated by DFT.

adapt and remain conformally in contact with Li even with volume change while cycling. Scanning electron microscopy (SEM) reveals that the conformal DSN coating indeed remained as a protection layer with Li deposition underneath even after long-term cycling (Figure S7). Consistent with the liquid-like behavior of DSN, differential scanning calorimetry (DSC) of DSN shows a low glass transition temperature (T_g) of −47°C (Figure 2D). In contrast, both B-FTEG and Si-FTEG show no flowability in the available frequency sweeping range and behave as elastic solids (Figures 2B and 2C). A high T_g of 50°C was observed for B-FTEG while the T_g was undetectable for covalently cross-linked Si-FTEG.

To show the dynamic nature, a hole with ~200 μm diameter was pierced through a thin film of each material and the film was left to heal at room temperature (RT) for 12 h (Figures 2E and S8). The hole of DSN was completely healed, while there was no change in the size or appearance for B-FTEG or Si-FTEG. We attribute the dynamic property of DSN to the reversible Al-OR coordination bonds reported previously.[46,47,50,51] Density functional theory (DFT) calculations were conducted on simplified Al-FTEG (DSN), B-FTEG, and Si-FTEG consisting of one FTEG chain bound with two $M(OCH_3)_3$ (M = Al, B, or Si) segments (Figure S9). The calculated coordination bonding energy of Al-O bond is found to be much lower than that of the B-O bond and Si-O bond, consistent with the finding that the Al-O bonds are weak and dynamic (Figure 2F). The FTIR of DSN exposed to humidity over time shows a continuous increase in the -OH vibration peak accompanied by a decrease in the Al-OR vibration peak, indicating facile bond hydrolysis (Figure S10). Despite the dynamic nature of the Al-O bonds, the DSN is robust enough to maintain its chemical structure in a battery, as indicated by FTIR of DSN after Li deposition in a battery (Figure S11).

Please cite this article in press as: Yu et al., A Dynamic, Electrolyte-Blocking, and Single-Ion-Conductive Network for Stable Lithium-Metal Anodes, Joule (2019), https://doi.org/10.1016/j.joule.2019.07.025

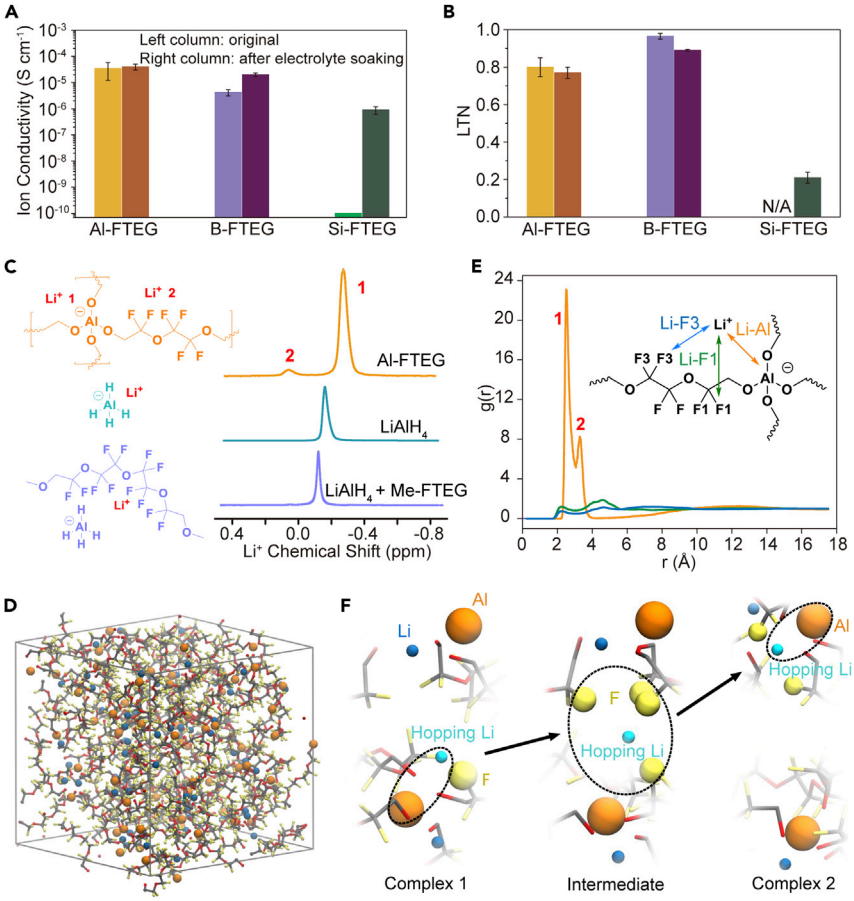

Figure 3. Electrochemical Characterization of DSN Derivatives and MD Simulation

(A and B) Ion conductivity (A) and Li transference number (LTN) measurement (B) of the DSN derivatives. For each material, left column is the original value without any addition of salt or electrolyte, while right column is the value after soaking in electrolyte. Soaking was done in 1 M $LiPF_6$ in EC/DEC (v:v = 1:1) with 10 wt % FEC additive for 24 h. Error bars represent standard deviation of measurements from at least three samples.

(C) The ^{7}Li-NMR spectra of DSN (orange), $LiAlH_4$ (cyan), and $LiAlH_4$ plus Me-FTEG (light violet), respectively.

(D) Visualization of the equilibrated DSN systems. Color scheme: Li^+ ions, blue; Al centers, orange; F atoms, yellow; C atoms, gray; O atoms, red. For clarity, all H atoms are omitted and FTEG chains are shown in stick format.

(E) Radial distribution functions at equilibrium. Orange, Li-Al; olive, Li-F1; blue, Li-F3.

(F) Li^+ ion transport pathway. The hopping Li^+ ion is shown in light blue while irrelevant Li^+ ions are dark blue. F atoms within 3 Å of the hopping Li are emphasized with yellow spheres. For clarity, FTEG chains are faded.

Li-Ion Conduction

It has been reported previously that high Li^+ ion conductivity and high Li transference number (LTN) of the SEI can help increase critical Li nucleate size, render smooth Li deposition, and reduce parasitic reactions of anions with Li metal.[6,17,44,45] Electrochemical impedance spectroscopy (EIS) measurements show considerable ion conductivity for DSN ($3.5 \pm 2.3 \times 10^{-5}$ S cm^{-1}) and B-FTEG ($4.2 \pm 1.1 \times 10^{-6}$ S cm^{-1}) at 25°C without addition of any salt or electrolyte (Figures 3A and S1), both of which are essentially high for interfacial ion conduction.[13,52] Consistent with our design, Si-FTEG shows negligible ion conductivity due to lack of free-ions in the network (<10^{-10} S cm^{-1}, Figure S2). On the other hand, the Si-FTEG became

Please cite this article in press as: Yu et al., A Dynamic, Electrolyte-Blocking, and Single-Ion-Conductive Network for Stable Lithium-Metal Anodes, Joule (2019), https://doi.org/10.1016/j.joule.2019.07.025

considerably more conductive after soaking in the electrolyte used for battery testing (1 M $LiPF_6$ in EC/DEC (v:v = 1:1) with 10 wt % FEC additive). Furthermore, the LTNs of DSN and B-FTEG were measured using potentiostatic polarization[53] in Li||Li symmetric cells, showing a LTN over 0.80 $\pm$ 0.05 for DSN and 0.96 $\pm$ 0.01 for B-FTEG (Figures 3B and S1). The slightly lower LTN of DSN compared to B-FTEG is expected due to the flowable nature of DSN which allows for a small degree of anion motion. Even after soaking in electrolyte, both showed only a slight decrease in LTN, confirming that they act as single-ion-conducting SEIs, but for Si-FTEG, the LTN after electrolyte soaking is 0.21 $\pm$ 0.03, similar to the normal liquid electrolyte[53] (Figures 3B, S12, and S13).

To further examine the ion transport behavior, molecular dynamic (MD) simulations were conducted on Al-FTEG (DSN). The simulated network forms a uniform distribution of Li atoms, Al centers, and FTEG chains (Figure 3C). It is worth noting that the radial distribution function (RDF) of Li-Al showed two peaks, giving one type of Li^+ ions (peak 1) close to Al anion centers and the other type (peak 2) far away (Figure 3D). We hypothesized that this could result from the presence of two Li^+ ion solvation environments in DSN. To confirm this, ^{7}Li-NMR was utilized to study Li^+ ion solvation in DSN. As shown in Figure 3E, indeed two ^{7}Li peaks can be found in DSN, labeled as 1 and 2, which represent two different Li^+ ion solvation states. However, for the $LiAlH_4$ precursor, there is only one ^{7}Li peak. Furthermore, using the RDF of Li-Al and the ^{7}Li-NMR spectra, we identified two different Li solvation environments in DSN: one is from Li^+ ions coordinated close to the $Al(OR)_4^-$ center, and the other is from Li^+ ions coordinated by the FTEG chains. The upfield peak (peak 1) in ^{7}Li-NMR is attributed to the Li^+ ions that are coordinated by the strongly-shielding $Al(OR)_4^-$ anions (Figures 3D and 3E). The Li^+ ions corresponding to the small peak 2 in DSN (Figures 3D and 3E) are assigned to Li^+ ions solvated by FTEG chains. The poor solvation ability of fluorinated ether chains results in deshielded Li^+ ions, causing a downfield shift and freeing of Li^+ ions to transport rapidly through the fluorinated chains. We thus took F atoms as an indicator of the FTEG chains to cross-validate this argument. The ^{19}F-NMR spectra (Figure S3) of DSN and B-FTEG support these observations by showing two sets of ^{19}F signals; one set comes from uncoordinated F atoms and the other comes from F atoms coordinated by Li^+ ions. Si-FTEG and FTEG, which do not contain any Li^+ ions, showed only one set of ^{19}F peaks as expected. The ^{19}F-NMR results are consistent with RDF of Li-F as well (Figure 3D). To further confirm this assignment, we synthesized an unreactive dimethyl terminated FTEG (Me-FTEG, Supplemental Information Synthesis) and conducted ^{7}Li-NMR on Me-FTEG mixed with 0.5 equivalence of $LiAlH_4$. This mixture showed obvious downfield shift for the ^{7}Li peak compared to neat $LiAlH_4$, which confirms the deshielding effect from FTEG chains. Similar shifts were observed from ^{7}Li-NMR spectra of lithium bis(trifluoromethanesulfonyl)imide (LiTFSI) compared to an LiTFSI/Me-FTEG mixture (Figure S14). Using these peak assignments, it is reasonable to conclude that Li^+ ion transport through DSN occurs via FTEG-mediated hopping between Al centers.

Figure 3F illustrates the simulated Li^+ ion hopping mechanism in DSN. At first, the hopping Li^+ ion is mainly bound by the lower Al center to form Complex 1, where the Li-Al distance is 3.2 Å (black circle in Complex 1). The hopping Li^+ ion then moves up to suspend between Al centers, leading to a Li-Al distance of ~4.2 Å. During the transition, the Li^+ ion is coordinated and transiently stabilized by the FTEG chain. The black circle in the intermediate panel of Figure 3F illustrates the transport through the intermediate state by highlighting the proximity of hopping Li^+ ion (cyan) to the F atoms (yellow), where the Li-F distances are below 3 Å. Finally, it can further hop to coordinate with the upper Al centers (black circle in Complex 2), forming

Please cite this article in press as: Yu et al., A Dynamic, Electrolyte-Blocking, and Single-Ion-Conductive Network for Stable Lithium-Metal Anodes, Joule (2019), https://doi.org/10.1016/j.joule.2019.07.025

Complex 2, the successfully hopped product. On the other hand, it is also possible for the hopping Li^+ ion to return and bind back with the lower Al center, in which it does not get over transition state barrier (Figure S15). Both the experimental and simulation results suggest that the fluorinated chains assist the transport of Li^+ ions.

Li-Metal Deposition and Morphology

Next, we examined the battery performance of Al-FTEG (DSN), B-FTEG, and Si-FTEG as artificial SEIs by monitoring the CE of Li stripping and plating in Li||Cu cells in a widely used commercial carbonate electrolyte (1 M $LiPF_6$ in EC/DEC (v:v = 1:1) with 10 wt % FEC additive) (Figure 4A). The sample with no artificial SEI coating rapidly loses its CE, lasting just over 80 cycles before failure. The Si-FTEG coated Cu cell, with neither single-ion conductivity nor dynamic property behavior, shows almost no improvement compared to the bare Cu control. By contrast, the single-ion-conductive yet non-dynamic B-FTEG modified Cu evidently prolongs the cycle life. This result supports our initial hypothesis that uniform single-ion conduction can reduce "hot spot" formation and enhance artificial SEI performance. Finally, with Al-FTEG (DSN) as an artificial SEI, the cyclability is vastly improved, lasting remarkably longer than uncoated, Si-FTEG, or B-FTEG samples. At 1 mA cm^{-2} current density and 1 mAh cm^{-2} capacity, the CE of the DSN-coated cell was maintained at ~94.9% for over 250 cycles.

DSN (Al-FTEG) and B-FTEG artificial SEIs can be directly coated on Li-metal foil and provide stable cycling in a Li||Li cell configuration. Both EIS measurements show much lower SEI impedances compared to the Si-FTEG or bare one (Figures 4B–4E). With resting time, the DSN (and B-FTEG) cell impedance increases modestly for only ~300 Ω in the first 8 h after cell assembling and then remains constant (Figures 4B and 4C). The impedance of the Si-FTEG or bare Li cell, on the other hand, increases dramatically from ~1,000 to over 3,000 Ω after 8 h and continues to increase even several days after assembling (Figures 4D, 4E, and S36). As a result, DSN Li||DSN Li and bare Li||bare Li cells were chosen as representatives to evaluate the overpotential, and the DSN cell show lower overpotential and more stable cycling than its counterpart (Figures 4F and S16), indicating its protection effect on Li-metal surface. High interfacial impedance and overpotential are known to be due to continuous electrolyte consumption to form a poorly conductive and devastated SEI.[6,15,37] To confirm this in our system, we checked the X-ray photoelectron spectroscopy (XPS) profiles of different SEI layers on Li (Figures 4G and S17). Careful scrutiny of XPS spectra reveals that the SEI of DSN Li and B-FTEG Li is dominated by FTEG chains (-CF_2-, ~693 eV, F 1s; -CF_2-O-, ~539 eV, O 1s), whereas that of Si-FTEG Li and bare Li contains more inorganic components derived from reactions between Li and electrolyte, such as $LiPF_6$ (~690 eV, F 1s), $Li_xPO_yF_z$ (~687 eV, F 1s; ~58 eV, Li 1s; ~535 eV, O 1s), LiF (~56 eV, Li 1s), and Li_2CO_3 (~533 eV, O 1s). These results suggest that the Al-FTEG (DSN) is the most effective, followed by the B-FTEG, to mitigate the electrolyte penetration and prevent continuous reactions between Li and electrolyte while the Si-FTEG coating or uncoated Li cannot. The Lewis acidity of the Si centers in the Si-FTEG may attract $LiPF_6$ in the electrolyte while the anionic centers in the DSN and B-FTEG mitigate the electrolyte penetration. This hypothesis is further supported by the swelling test where less swelling was observed for the soaked DSN and B-FTEG, and by the ^{19}F-NMR where less $LiPF_6$ was found in the soaked DSN and B-FTEG (Figure S18). The lower initial SEI impedance of the DSN and B-FTEG-coated cell (~600 Ω) compared to that of the Si-FTEG and bare Li cell (~1,000 Ω) can be explained by the electrolyte-blocking property as well (Figures 4B–4E).

Previous literature[22,24–26,54] has shown that non-dendritic 2D growth of Li is desirable for battery performance; thus, we used SEM to examine the morphology of Li

Please cite this article in press as: Yu et al., A Dynamic, Electrolyte-Blocking, and Single-Ion-Conductive Network for Stable Lithium-Metal Anodes, Joule (2019), https://doi.org/10.1016/j.joule.2019.07.025

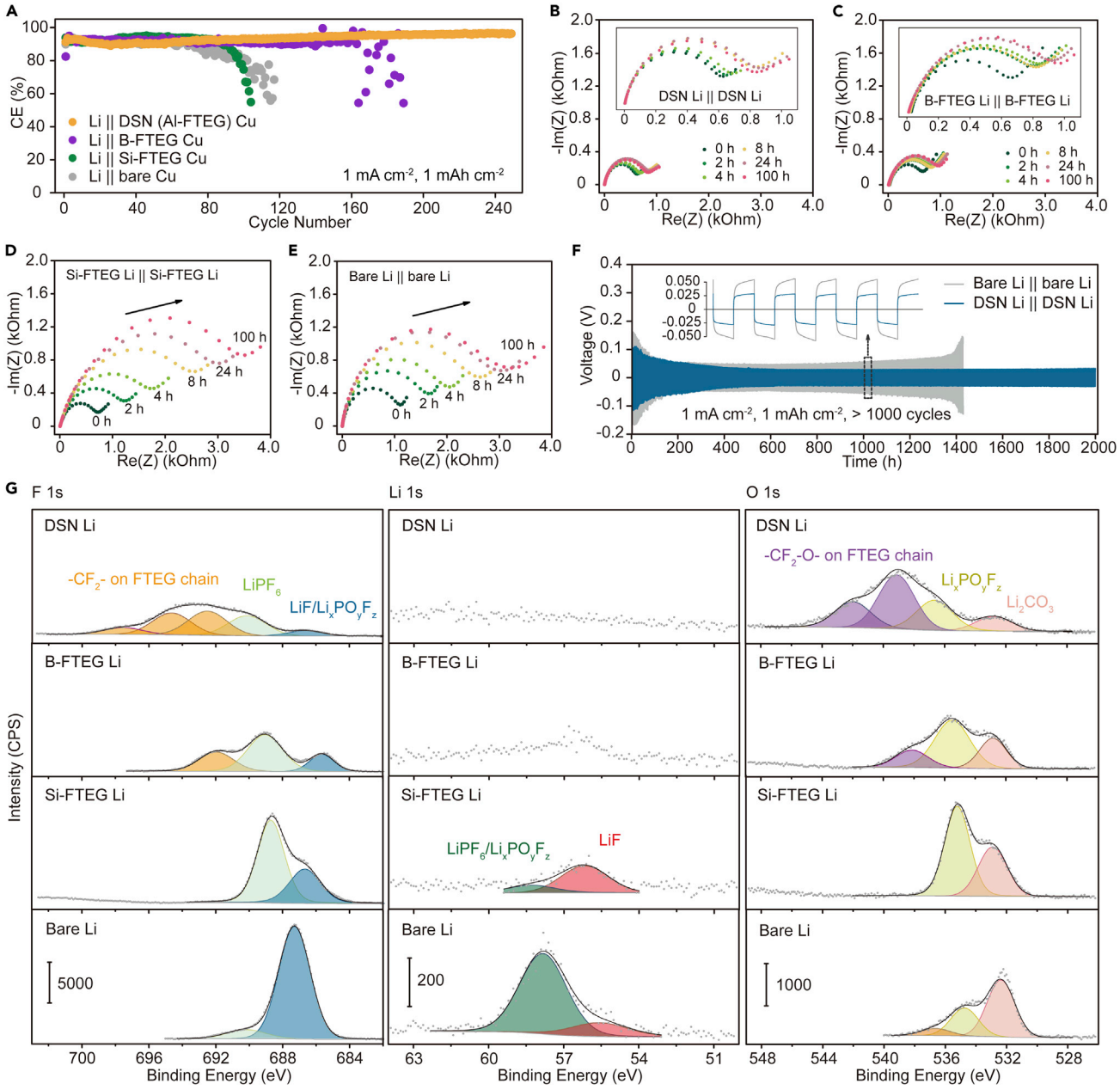

Figure 4. Study of Artificial SEIs

(A) Cycle stability plot of Coulombic efficiency (CE) under 1 mA cm^{-2} current density and 1 mAh cm^{-2} areal capacity. The electrolyte is 1 M $LiPF_6$ in EC/DEC (v:v = 1:1) with 10 wt % FEC additive. 75 μL electrolyte was used for each cell.

(B–E) Nyquist plot of DSN Li||DSN Li (B), B-FTEG Li||B-FTEG Li (C), Si-FTEG Li||Si-FTEG Li (D), and bare Li||bare Li (E) symmetric cell rested over time after cell assembling. Inset of (B) and (C): zoomed-in plot.

(F) Comparison of cycling performance of bare Li||bare Li and DSN Li||DSN Li symmetric cells. Inset: zoomed-in plot of the 500^{th}–505^{th} cycles.

(G) F 1s, Li 1s, and O 1s XPS profiles of different artificial SEIs coated Li and bare Li after soaking in the electrolyte for 4 days followed by washing coating layers off. CPS, counts per second. Scale bars: F 1s, 5,000 CPS; Li 1s, 200 CPS; O 1s, 1,000 CPS.

deposition on Cu to further understand the origins of the improved cyclability of Li metal with the DSN coating. The DSN protection layer remained nearly intact after 1 mAh cm^{-2} Li deposition despite being deliberately peeled off for side-view SEM (Figures 5A, 5B, and S7). We then washed off the top layer in order to compare the Li morphology. With the DSN protection, the deposited Li at 1 mAh cm^{-2}

Please cite this article in press as: Yu et al., A Dynamic, Electrolyte-Blocking, and Single-Ion-Conductive Network for Stable Lithium-Metal Anodes, Joule (2019), https://doi.org/10.1016/j.joule.2019.07.025

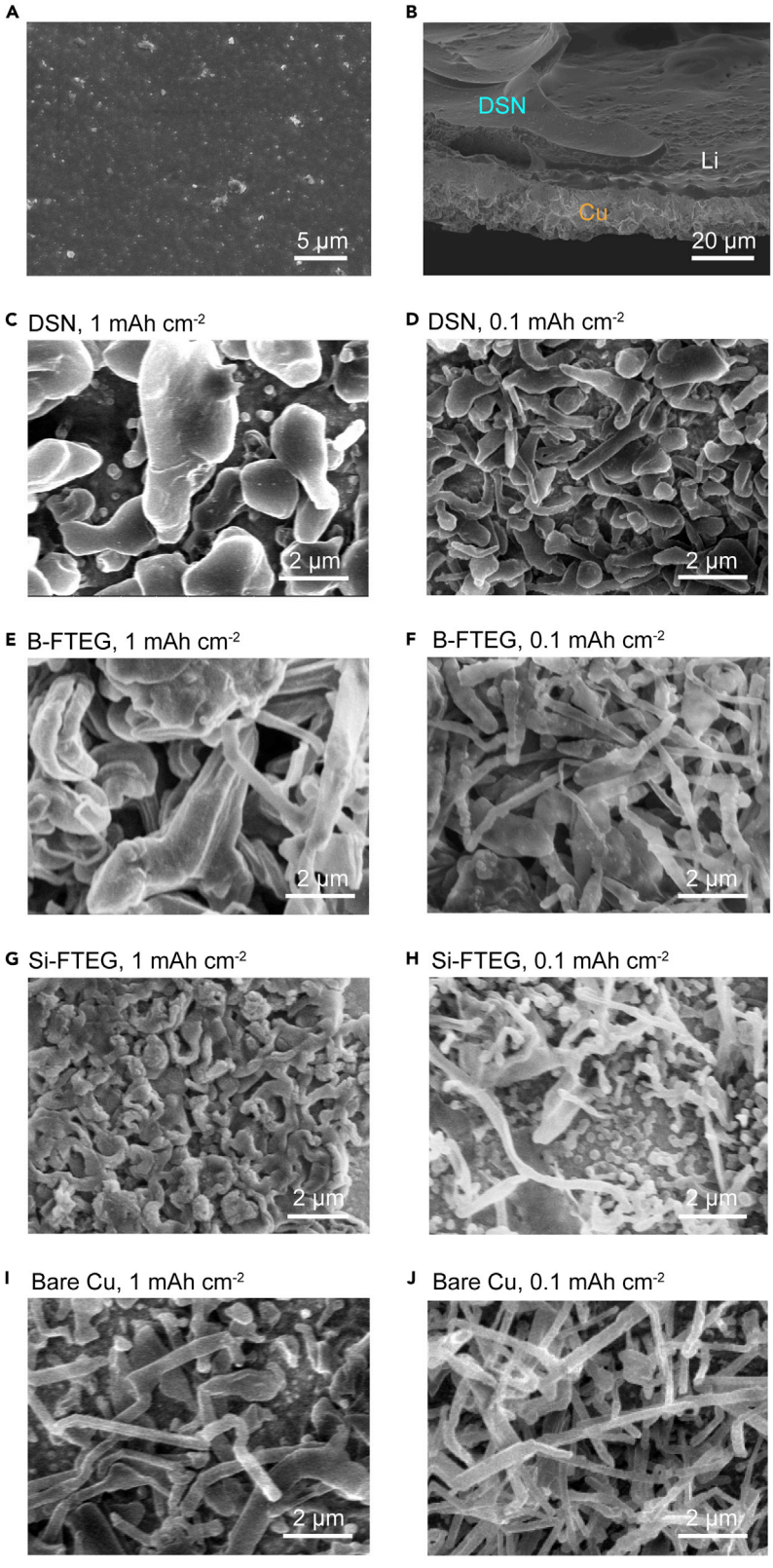

Please cite this article in press as: Yu et al., A Dynamic, Electrolyte-Blocking, and Single-Ion-Conductive Network for Stable Lithium-Metal Anodes, Joule (2019), https://doi.org/10.1016/j.joule.2019.07.025

Figure 5. Li Deposition Morphology

(A) Top view SEM of the DSN layer with directly deposited 1 mAh cm^{-2} Li underneath. Scale bar, 5 μm.

(B) Side view of deposited 0.5 mAh cm^{-2} Li under the protection of DSN. Scale bar, 20 μm.

(C–J) Morphology of Li deposited on bare Cu and different artificial SEI coated Cu foils. (C) DSN, 1 mAh cm^{-2}. (D) DSN, 0.1 mAh cm^{-2}. (E) B-FTEG, 1 mAh cm^{-2}. (F) B-FTEG, 0.1 mAh cm^{-2}. (G) Si-FTEG, 1 mAh cm^{-2}. (H) Si-FTEG, 0.1 mAh cm^{-2}. (I) bare, 1 mAh cm^{-2}. (J) bare, 0.1 mAh cm^{-2}. Scale bars, 2 μm.

showed large and flat plate-like structures, while Li deposited with B-FTEG coating showed large particles mixed with needle-like dendrites (Figures 5C, 5E, S19, and S20). Interestingly, the initial Li deposits at 0.1 mAh cm^{-2} under DSN were still dominated by 2D plates whereas those under B-FTEG were mainly 1D dendritic structures (Figures 5D and 5F). In contrast, for Si-FTEG coated Cu or bare Cu, the deposited Li were observed as needles or small particles at both 1 and 0.1 mAh cm^{-2} (Figures 5G–5J). The best Li surface protection effect of the DSN coating, confirmed by the least Li||Li interfacial impedance evolution over time (Figures 4B and 4C) and fewest products of parasitic reactions between Li and electrolyte (Figure 4G), is potentially a critical factor that helped to improve the Li deposition morphology. The non-dynamic B-FTEG was observed to be less effective due to the absence of flowability and conformal protection. On the other hand, the continuous increase observed in Li||Li impedance of Si-FTEG-coated Li or bare Li (Figures 4D and 4E) along with the lack of conformal protection is responsible for its worse Li deposition morphology. These SEM observations are consistent with the Li||Cu cycling result (Figure 4A) and confirm that the DSN design improves Li growth morphology.

Battery Performance

Given the improved Li deposition morphology with DSN, we further investigated the Li stripping and plating performance with the DSN artificial SEI. The Li||DSN Cu cell can stably cycle for over 400 cycles with a high average CE of ~97.3% at a current density of 0.25 mA/cm^2 and areal capacity of 0.5 mAh cm^{-2} (Figure 6A). At a current density of 0.5 mA cm^{-2} and a capacity of 1 mAh cm^{-2}, the CE of DSN-coated cell remains at ~96.5% for over 400 cycles (Figures S21 and S35). The cycle number and CE outperform those of other artificial SEIs or strategies using 1M $LiPF_6$ in carbonate electrolytes (Figure 6B and Table S1). Under other electrolytes or higher current density conditions, DSN-coated cells also perform significantly better than bare ones (Figure S21). The voltage profiles of Li||DSN Cu cell suggest stable stripping and plating by showing a smooth plateau with a low overpotential of ~20 mV (Figure 6C). The high CE and stable cycling are indications of chemical stability of DSN against Li metal. The cyclic voltammetry (CV) of Li||coated Cu cell in previous reports[37,38] usually contain several redox peaks aside from Li stripping and plating, indicating additional side reactions between the coating layer and Li metal. Nevertheless, the CV of the Li||DSN Cu cell showed clean sweep with no other peaks except those for Li stripping and plating, again confirming that DSN has no uncontrollable side reactions with Li metal (Figures 6D and S22). Such tolerance toward the highly reductive environment of Li metal makes DSN robust for long-term cycling.

An ideal artificial SEI will enable the operation of Li-metal full battery using all commercial components, especially thin Li foils and commercial cathodes with high active material proportion, for practical application. We were able to directly coat an DSN protection layer on a thin Li foil (42 μm thickness, ~8 mAh cm^{-2}) through a dip-coating method (Experimental Procedures and Figure S23) and assemble full cells with coated Li foils and commercial NMC532 electrode sheets with the industry standard (~95% active material, 2 mAh cm^{-2} loading). The DSN coating greatly decreases impedance while increasing the rate capability of Li||NMC full

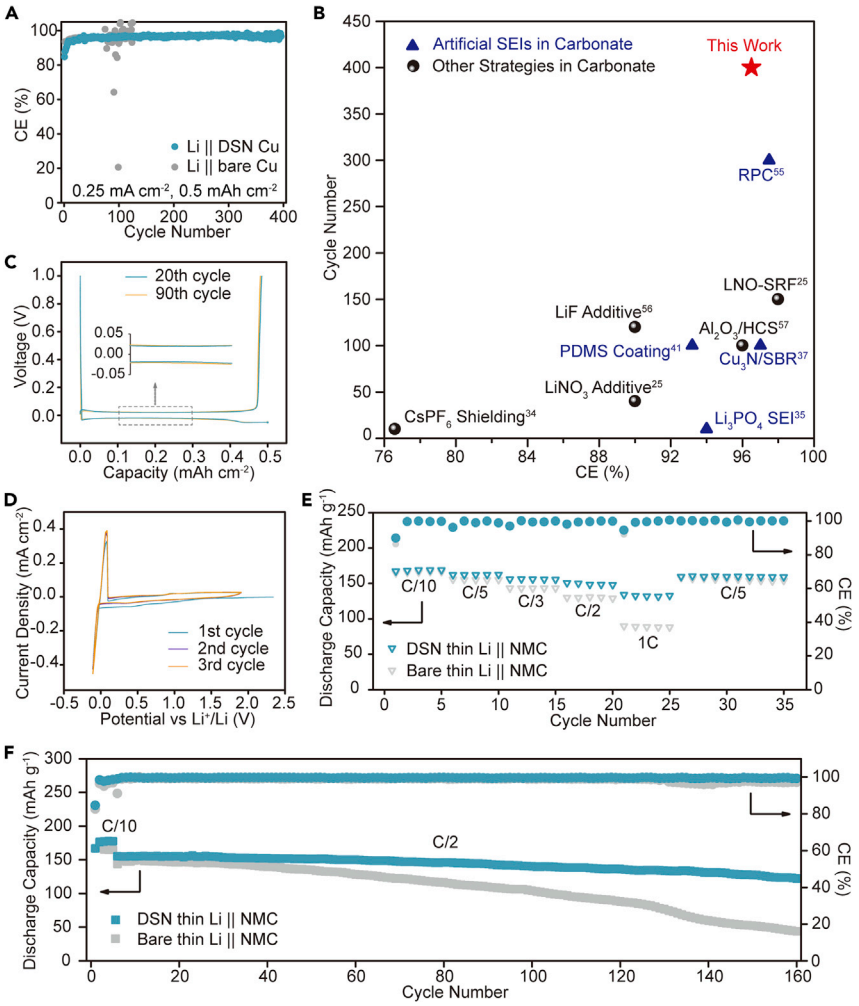

Figure 6. Battery Performance

(A) Cycle stability plot of CE at a current density of 0.25 mA cm^{-2} and areal capacity of 0.5 mAh cm^{-2}.

(B) Comparison of the Li||Cu cell cycle number and CE of this work (red star) with the performance of other artificial SEIs or strategies[25,34,35,37,41,55–57] using 1M $LiPF_6$ in carbonate electrolytes at 0.5 mA cm^{-2} and 1 mAh cm^{-2}. Dark blue triangles: previous artificial SEIs; black spheres: other strategies.

(C) Voltage profiles of Li||DSN Cu cell at the 20th (cyan) and 90th (orange) cycle, at a current density of 0.25 mA cm^{-2} and areal capacity of 0.5 mAh cm^{-2}.

(D) The first three cyclic voltammetry (CV) cycles of Li||DSN Cu cell (voltage range: −0.1 V to 2.0 V; scanning rate: 0.5 mV s^{-1}).

(E) Rate capability of DSN thin Li (42 μm)||NMC532 (cyan) and bare thin Li||NMC532 (gray) full batteries.

(F) Long-term cycling performance of DSN thin Li||NMC532 (cyan) and bare thin Li||NMC532 (gray) full batteries.

cells, obtaining a discharge capacity of 132.9 mAh g^{-1} compared to 88.2 mAh g^{-1} for the uncoated anodes at a rate of 1C (Figures 6E, S24, and S25). Given a higher average CE (>99.6%), the DSN Li||NMC full cell also showed much improved capacity retention of ~85% after 160 cycles at a charge-discharge rate of C/2 as compared to that of the bare Li cell (<30% retention). The average CE of the bare Li battery is only ~98.4% due to the dramatic failure after 130 cycles (Figures 6F, S25, and S26).

Please cite this article in press as: Yu et al., A Dynamic, Electrolyte-Blocking, and Single-Ion-Conductive Network for Stable Lithium-Metal Anodes, Joule (2019), https://doi.org/10.1016/j.joule.2019.07.025

These results demonstrate that DSN is promising for large-scale fabrication and further development into pouch or cylinder cells.

Conclusions

In this work, we provide the first demonstration of utilizing Al-OR bonding to create a dynamic single-ion-conductive network (DSN) coating to protect Li-metal anodes. The DSN greatly improves Li-metal-anode performance mainly in three ways: (1) its appreciable Li^+ single ion conductivity can reduce the interfacial impedance and lower the overpotential for Li-metal deposition, (2) the DSN coating mitigates the electrolyte penetration and reduces parasitic reactions between Li and electrolyte, (3) the dynamic flowability results in relatively uniform Li-metal deposition morphology, and (4) the chemically inert FTEG chains makes DSN coating stable toward Li metal. All features enable stable Li-metal cycling in Li||Li symmetric cells, Li||Cu half cells, and Li||NMC full cells. Specifically, the electrodes and electrolyte utilized in Li||NMC full cells are commercially available at a large-scale. Combined with its low-cost starting materials and convenient processing method, our reported DSN coating provides a promising approach for realizing practical Li-metal batteries. Meanwhile, our design strategy to combine single-ion conductivity with dynamic chemistry into one material matrix provides an extraordinary type of material for next generation Li batteries.

EXPERIMENTAL PROCEDURES

Synthesis of DSN, B-FTEG, and Si-FTEG

DSN Synthesis

410 mg FTEG and 2.8 mL DME were added to a 20 mL vial. After sonicating for 3 min until FTEG was fully dissolved, the vial was transferred into a nitrogen-filled glovebox with sub-ppm O_2 and H_2O level (MBRAUN). Under stirring, 500 μL 1 M $LiAlH_4$ in THF was added dropwise into the vial. After stirring at RT overnight, the yielding solution was filtered through 0.45 μm PTFE filter into 4 mL vial, to obtain ~150 mg mL^{-1} DSN/DME solution.

B-FTEG Synthesis

410 mg FTEG and 2.8 mL DME were added o ta 20 mL vial. After sonicating for 3 min until FTEG was fully dissolved, the vial was transferred into the nitrogen-filled glovebox. While stirring, 250 μL 2 M $LiBH_4$ in THF was added dropwise into the vial. The yielding solution was immediately filtered through 0.45 μm PTFE filter into 4 mL vial, to obtain ~150 mg mL^{-1} of B-FTEG in DME solution.

Si-FTEG Synthesis

410 mg FTEG and 3.2 mL DME were added to a 20 mL vial. After sonicating for 3 min until FTEG was fully dissolved, the vial was transferred into the nitrogen-filled glovebox. Under stirring, 85 mg $SiCl_4$ was added slowly into the vial and the vial was sealed then. After stirring at 80°C overnight, the yielding solution was filtered through 0.45 μm PTFE filter into 4 mL vial, to obtain ~150 mg mL^{-1} Si-FTEG/DME solution. All those solutions were used for spin-coating right after procurement. For free-standing samples, the solutions were poured into corresponding mold and heated to 80°C for 6 h to evaporate all solvents.

Fabrication of DSN, B-FTEG, and Si-FTEG-Modified Cu Electrodes and DSN-Coated Li Anode

The coated Cu working electrodes were fabricated in the nitrogen-filled glovebox. About 100 μL as-synthesized DSN (or B-FTEG, Si-FTEG)/DME solution (~150 mg mL^{-1}) was transferred onto the smooth side of Cu foil (~2 cm^2 round

Please cite this article in press as: Yu et al., A Dynamic, Electrolyte-Blocking, and Single-Ion-Conductive Network for Stable Lithium-Metal Anodes, Joule (2019), https://doi.org/10.1016/j.joule.2019.07.025

disk) and spin-coated with 2000 rpm spin rate for 30 s. The acceleration rate is 500 rpm s^{-1}. The obtained modified Cu electrodes were transferred quickly into an argon-filled glovebox with sub-ppm O_2 and H_2O level (Vigor Tech) for further use. The coated thin Li foil was fabricated with dip-coating method in an argon-filled glovebox with sub-ppm O_2 and H_2O level (Vigor Tech). First, thin Li foils were punched into ~0.7 (for Li||Cu cells) or 1.0 (for Li||Li and Li||NMC cells) cm^2 round disks. Then they were dipped into ~50 mg mL^{-1} DSN/DME solution for 1 min and lifted out. The remaining solution on Li was immediately but gently wiped out with Kimwipes (KIMTECH) until a dry yet sticky surface was formed.

DFT Calculations

The molecular geometries for the ground and charged states were optimized by density functional theory (DFT) at the B3LYP/6–31G+(d,p) level. Then, the energy of molecules were evaluated at the DFT-B3LYP/6–31G+(d,p). The bonding energy was calculated from the energy difference between starting structure and products after bond breakage. All the DFT calculations were carried out with the Gaussian 09 package.

MD Simulations

All-atom MD simulations of FTEG-DSN were performed in GROMACS (Figures S27–S30 and Tables S3–S7). Force field parameters were generated using AMBER methodology with the Force Field Toolkit in VMD. Production simulations were performed in triplicate for each network in the NPT ensemble for 50 ns, in both the absence and presence of electric field. A timestep of 1 ns was used in all simulations. Each simulation contained 128 FTEG chains, 64 Al atoms, and 64 Li atoms. Systems were initialized without Li atoms or bonds between FTEG chains and Al atoms. Network topology was generated dynamically to best replicate experimental conditions; the linking procedure is detailed in the Supplemental Information. Initial configurations consisted of Al atoms and FTEG chains randomly distributed in the gas phase. The system was first energy-minimized in the NVE ensemble, then equilibrated in the NVT and NPT at 600 K and 1 bar, resulting in an average density of (~1,700 g/cm^3). Bondings were then generated between FTEG chains and Al atoms. Next, Li atoms were added and the system re-equilibrated in the NPT ensemble. Production simulations utilized Parrinello-Rahman barostat and Nosë-Hoover thermostat. Simulations of Li transport under applied voltage used potentials of strength between 1 and 6 V/nm along the z axis. Analysis of MD trajectories was aided by use of the MDAnalysis library in Python.

Material Characterizations

^1H NMR spectra were recorded on a Varian Mercury 400 MHz NMR spectrometer and ^7Li NMR spectra were recorded on a UI 300 MHz NMR spectrometer at RT. For ^7Li NMR spectra, in order to rule out concentration effects, we fixed the concentration of Li^+ ion in THF at ~0.15 M for all samples. Rheological experiments were carried out using an Ares G2 Rheometer (TA Instruments) with an advanced Peltier system (APS) at 25°C. Frequency sweeps were carried out from 0.01 to 1000 Hz at 0.1% strain. Stress-strain tests were carried out using Instron with a 10 mm/min strain rate. DSC experiments were performed using a DSC-Q2000 (TA Instruments) over a temperature range of −80 to 100°C with a ramp rate of 10°C min^{-1}. TGA plots were recorded with a Mettler Toledo AG-TGA/SDTA851e (Figure S31). A FEI Magellan 400 XHR SEM was used for SEM and Energy dispersive spectroscopy (EDS) characterizations. XPS profiles were collected by PHI VersaProbe 1 Scanning XPS Microprobe. The samples were transferred for XPS using a sample transfer vessel that prevented air exposure at any time. Before XPS measurement, the artificial SEIs coated or bare Li was soaked in the electrolyte for 4 days, and then washed with DME for 30 min to remove electrolyte and coating layers. FTIR spectra were measured using a Nicolet iS50 FT/IR

Spectrometer (Thermo Fisher) with a diamond ATR attachment. For flammability test, we burned the material under fire for 10 s and stopped to observe (Figure S37).

Electrochemical Measurements

All battery components used in this work were commercial large-scale products and electrochemical testing was all carried out in 2032-type coin cell configuration. 1.0 M $LiPF_6$ in EC/DEC electrolyte (Selectilyte LP40) and FEC (MONOFLUOROETHYLENE CARBONATE) were purchased from BASF. One layer of Celgard 2325 (25 μm PP/PE/PP) was used as separator and 75 μL electrolyte was added in each coin cell. Thin Li foil (~42 μm) was purchased from Hydro-Québec. Two layers of thin Li foils were stacked, punched, and used in Li||Cu half cell for cycling, and one layer of that was used in Li||NMC full cell. Single-side coated $LiNi_{0.5}Mn_{0.3}Co_{0.2}O_2$ (NMC532) sheets (~95% active materials) with ~2 mAh cm^{-2} capacity loading were purchased from MTI. Thick Li foil (750 μm) was purchased from Alfa Aesar and used in Li||Li symmetric cell and Li||Cu cell for SEM. Copper current collector (25 μm, 99.8% metals basis) was purchased from Alfa Aesar and used as working electrode. The EIS, LTN, and CV measurements were carried out on a Biologic VMP3 system. The cycling tests for half cells and full cells were carried out on an Arbin system. The EIS measurements were taken over a frequency range of 100 mHz to 7 MHz. For the LTN measurements, we added 5w.t.% diglyme to wet the DSN film to get lower resistance and 100 mV constant voltage bias was applied to Li||Li cells. The CV tests were carried out over a voltage range of -0.1 to 2 V for three cycles. For Li||Cu half-cell CE cycling tests, ten pre-cycles between 0 and 1 V were initialized to clean Cu electrode surface, and then cycling was done by depositing 1 (or 0.5) mAh cm^{-2} of Li onto Cu electrode followed by stripping to 1 V. The average CE is calculated by dividing the total stripping capacity by the total deposition capacity after the formation cycle. For CE test (Figure S32), a standard protocol was followed: (1) perform one initial formation cycle with Li deposition of 5 mAh cm^{-2} on Cu under 0.5 mA cm^{-2} current density and stripping to 1 V; (2) deposit 5 mAh cm^{-2} Li on Cu under 0.5 mA cm^{-2} as Li reservoir; (3) repeatedly strip and plate Li with 1 mAh cm^{-2} under 0.5 mA cm^{-2} for 10 cycles; (4) strip all Li to 1 V. For the Li||NMC full cell study, NMC532 sheets were used and stored in argon-filled glovebox as received. After the first five activation cycles at C/10 charge/discharge, the cells were cycled at C/2 between 2.7 to 4.2 V.

SUPPLEMENTAL INFORMATION

Supplemental Information can be found online at https://doi.org/10.1016/j.joule.2019.07.025.

ACKNOWLEDGMENTS

This work is supported by the US Department of Energy, under the Assistant Secretary for Energy Efficiency and Renewable Energy, Office of Vehicle Technologies, the Battery Materials Research (BMR) Program, and Battery 500 Consortium. Part of this work was performed at the Stanford Nano Shared Facilities (SNSF), supported by the National Science Foundation under award ECCS-1542152. D.G.M. acknowledges support by the National Science Foundation Graduate Research Fellowship Program under Grant No. DGE-114747. C.V.A. acknowledges the TomKat Center Postdoctoral Fellowship in Sustainable Energy at Stanford.

AUTHOR CONTRIBUTIONS

Z.Y., D.G.M., and Z.B. conceived the idea. Z.Y., D.G.M., and Z.B. designed the experiments. Y.C. and Z.B. directed the project. Z.Y. performed the material preparation and chemical characterization. D.G.M. performed the ^{7}Li-NMR. W.M. and J.Q.

performed MD simulations and rationales. M.L., Y.T., and S.C. performed the SEM experiments. C.V.A. performed the XPS experiments. Z.Y. and D.G.M. conducted mechanical property tests and electrochemical measurements. Q.Z., X.Y., and J.K. helped with mechanical property tests. A.P., D.F., H.W., and K.L. helped with electrochemical measurements. All authors discussed and analyzed the data. Z.Y., D.G.M., Y.C., and Z.B. wrote the manuscript.

DECLARATION OF INTERESTS

This work has been filed as USA Provisional Patent No. 62/740,785.

Received: June 11, 2019
Revised: July 3, 2019
Accepted: July 24, 2019
Published: August 26, 2019

REFERENCES

1. Goodenough, J.B., and Kim, Y. (2010). Challenges for rechargeable Li batteries †. Chem. Mater. *22*, 587–603.
2. Janek, J., and Zeier, W.G. (2016). A solid future for battery development. Nat. Energy *1*, 16141.
3. Liu, K., Liu, Y., Lin, D., Pei, A., and Cui, Y. (2018). Materials for lithium-ion battery safety. Sci. Adv. *4*, eaas9820.
4. Goodenough, J.B., and Park, K.S. (2013). The Li-ion rechargeable battery: A perspective. J. Am. Chem. Soc. *135*, 1167–1176.
5. Choi, J.W., and Aurbach, D. (2016). Promise and reality of post-lithium-ion batteries with high energy densities. Nat. Rev. Mater. *1*, 16013.
6. Lin, D., Liu, Y., and Cui, Y. (2017). Reviving the lithium metal anode for high-energy batteries. Nat. Nanotechnol. *12*, 194–206.
7. Xu, W., Wang, J., Ding, F., Chen, X., Nasybulin, E., Zhang, Y., and Zhang, J.G. (2014). Lithium metal anodes for rechargeable batteries. Energy Environ. Sci. *7*, 513–537.
8. Bruce, P.G., Freunberger, S.A., Hardwick, L.J., and Tarascon, J.M. (2011). Li–O2 and Li–S batteries with high energy storage. Nat. Mater. *11*, 19–29.
9. Cheng, X.B., Zhang, R., Zhao, C.Z., and Zhang, Q. (2017). Toward safe lithium metal anode in rechargeable batteries: a review. Chem. Rev. *117*, 10403–10473.
10. Liu, Y., Zhou, G., Liu, K., and Cui, Y. (2017). Design of complex nanomaterials for energy storage: past success and future opportunity. Acc. Chem. Res. *50*, 2895–2905.
11. Tarascon, J.M., and Armand, M. (2001). Issues and challenge s facing rechargeable lithium batteries. Nature *414*, 359–367.
12. Lopez, J., Mackanic, D.G., Cui, Y., and Bao, Z. (2019). Designing polymers for advanced battery chemistries. Nat. Rev. Mater. *4*, 312–330.
13. Xu, K. (2014). Electrolytes and interphases in Li-Ion batteries and beyond. Chem. Rev. *114*, 11503–11618.
14. Wei, S., Choudhury, S., Tu, Z., Zhang, K., and Archer, L.A. (2018). Electrochemical interphases for high-energy storage using reactive metal anodes. Acc. Chem. Res. *51*, 80–88.
15. Cheng, X.B., Zhang, R., Zhao, C.Z., Wei, F., Zhang, J.G., and Zhang, Q. (2016). A review of solid electrolyte interphases on lithium metal anode. Adv. Sci. *3*, 1500213.
16. Xu, K. (2004). Nonaqueous liquid electrolytes for lithium-based rechargeable batteries. Chem. Rev. *104*, 4303–4417.
17. Tikekar, M.D., Choudhury, S., Tu, Z., and Archer, L.A. (2016). Design principles for electrolytes and interfaces for stable lithium-metal batteries. Nat. Energy *1*, 16114.
18. Liu, K., Pei, A., Lee, H.R., Kong, B., Liu, N., Lin, D., Liu, Y., Liu, C., Hsu, P.C., Bao, Z., et al. (2017). Lithium metal anodes with an adaptive "solid-liquid" interfacial protective layer. J. Am. Chem. Soc. *139*, 4815–4820.
19. Liu, Y., Tzeng, Y.-K., Lin, D., Pei, A., Lu, H., Melosh, N.A., Shen, Z.-X., Chu, S., and Cui, Y. (2018). An ultrastrong double-layer nanodiamond interface for stable lithium metal anodes. Joule *2*, 1595–1609.
20. Cohen, Y.S., Cohen, Y., and Aurbach, D. (2000). Micromorphological studies of lithium electrodes in alkyl carbonate solutions using in situ atomic force microscopy. J. Phys. Chem. B *104*, 12282–12291.
21. Monroe, C., and Newman, J. (2003). Dendrite growth in lithium/polymer systems. J. Electrochem. Soc. *150*, A1377.
22. Miao, R., Yang, J., Feng, X., Jia, H., Wang, J., and Nuli, Y. (2014). Novel dual-salts electrolyte solution for dendrite-free lithium-metal based rechargeable batteries with high cycle reversibility. J. Power Sources *271*, 291–297.
23. Fan, X., Chen, L., Borodin, O., Ji, X., Chen, J., Hou, S., Deng, T., Zheng, J., Yang, C., Liou, S.C., et al. (2018). Non-flammable electrolyte enables Li-metal batteries with aggressive cathode chemistries. Nat. Nanotechnol. *13*, 715–722.
24. Jiao, S., Ren, X., Cao, R., Engelhard, M.H., Liu, Y., Hu, D., Mei, D., Zheng, J., Zhao, W., Li, Q., et al. (2018). Stable cycling of high-voltage lithium metal batteries in ether electrolytes. Nat. Energy *3*, 739–746.
25. Liu, Y., Lin, D., Li, Y., Chen, G., Pei, A., Nix, O., Li, Y., and Cui, Y. (2018). Solubility-mediated sustained release enabling nitrate additive in carbonate electrolytes for stable lithium metal anode. Nat. Commun. *9*, 3656.
26. Zeng, Z., Murugesan, V., Han, K.S., Jiang, X., Cao, Y., Xiao, L., Ai, X., Yang, H., Zhang, J.-G., Sushko, M.L., et al. (2018). Non-flammable electrolytes with high salt-to-solvent ratios for Li-ion and Li-metal batteries. Nat. Energy *3*, 674–681.
27. Mogi, R., Inaba, M., Jeong, S.-K., Iriyama, Y., Abe, T., and Ogumi, Z. (2002). Effects of some organic additives on lithium deposition in propylene carbonate. J. Electrochem. Soc. *149*, A1578.
28. Xiong, S., Xie, K., Diao, Y., and Hong, X. (2014). Characterization of the solid electrolyte interphase on lithium anode for preventing the shuttle mechanism in lithium–sulfur batteries. J. Power Sources *246*, 840–845.
29. Choudhury, S., Mangal, R., Agrawal, A., and Archer, L.A. (2015). A highly reversible room-temperature lithium metal battery based on crosslinked hairy nanoparticles. Nat. Commun. *6*, 10101.
30. Manthiram, A., Yu, X., and Wang, S. (2017). Lithium battery chemistries enabled by solid-state electrolytes. Nat. Rev. Mater. *2*, 16103.
31. Feng, Y., Tan, R., Zhao, Y., Gao, R., Yang, L., Yang, J., Li, H., Zhou, G., Chen, H., and Pan, F. (2018). Insight into fast ion migration kinetics of a new hybrid single Li-ion conductor based on aluminate complexes for solid-state Li-ion batteries. Nanoscale *10*, 5975–5984.
32. Zhang, Z., Shao, Y., Lotsch, B., Hu, Y.S., Li, H., Janek, J., Nazar, L.F., Nan, C.W., Maier, J., Armand, M., et al. (2018). New horizons for inorganic solid state ion conductors. Energy Environ. Sci. *11*, 1945–1976.
33. Lu, Y., Tikekar, M., Mohanty, R., Hendrickson, K., Ma, L., and Archer, L.A. (2015). Stable

cycling of lithium metal batteries using high transference number electrolytes. Adv. Energy Mater. *5*, 1402073.

34. Ding, F., Xu, W., Graff, G.L., Zhang, J., Sushko, M.L., Chen, X., Shao, Y., Engelhard, M.H., Nie, Z., Xiao, J., et al. (2013). Dendrite-free lithium deposition via self-healing electrostatic shield mechanism. J. Am. Chem. Soc. *135*, 4450–4456.

35. Li, N.W., Yin, Y.X., Yang, C.P., and Guo, Y.G. (2016). An artificial solid electrolyte interphase layer for stable lithium metal anodes. Adv. Mater. *28*, 1853–1858.

36. Zhang, Y.J., Wang, W., Tang, H., Bai, W.Q., Ge, X., Wang, X.L., Gu, C.D., and Tu, J.P. (2015). An ex-situ nitridation route to synthesize Li3N-modified Li anodes for lithium secondary batteries. J. Power Sources *277*, 304–311.

37. Liu, Y., Lin, D., Yuen, P.Y., Liu, K., Xie, J., Dauskardt, R.H., and Cui, Y. (2017). An artificial solid electrolyte interphase with high Li-Ion conductivity, mechanical strength, and flexibility for stable lithium metal anodes. Adv. Mater. *29*, 1605531.

38. Zheng, G., Wang, C., Pei, A., Lopez, J., Shi, F., Chen, Z., Sendek, A.D., Lee, H.W., Lu, Z., Schneider, H., et al. (2016). High-performance lithium metal negative electrode with a soft and flowable polymer coating. ACS Energy Lett. *1*, 1247–1255.

39. Kim, M.S., Ryu, J.-H., Deepika, Lim, Y.R., Nah, I.W., Lee, K.-R., Archer, L.A., and Il Cho, W. (2018). Langmuir–Blodgett artificial solid-electrolyte interphases for practical lithium metal batteries. Nat. Energy *3*, 889–898.

40. Zhang, H., Liao, X., Guan, Y., Xiang, Y., Li, M., Zhang, W., Zhu, X., Ming, H., Lu, L., Qiu, J., et al. (2018). Lithiophilic-lithiophobic gradient interfacial layer for a highly stable lithium metal anode. Nat. Commun. *9*, 3729.

41. Zhu, B., Jin, Y., Hu, X., Zheng, Q., Zhang, S., Wang, Q., and Zhu, J. (2017). Poly(dimethylsiloxane) thin film as a stable interfacial layer for high-performance lithium-metal battery anodes. Adv. Mater. *29*, 1603755.

42. Zheng, G., Lee, S.W., Liang, Z., Lee, H.W., Yan, K., Yao, H., Wang, H., Li, W., Chu, S., and Cui, Y. (2014). Interconnected hollow carbon nanospheres for stable lithium metal anodes. Nat. Nanotechnol. *9*, 618–623.

43. Lopez, J., Pei, A., Oh, J.Y., Wang, G.N., Cui, Y., and Bao, Z. (2018). Effects of polymer coatings on electrodeposited lithium metal. J. Am. Chem. Soc. *140*, 11735–11744.

44. Pang, Q., Zhou, L., and Nazar, L.F. (2018). Elastic and Li-ion–percolating hybrid membrane stabilizes Li metal plating. Proc. Natl. Acad. Sci. USA *115*, 12389–12394.

45. Xu, R., Xiao, Y., Zhang, R., Cheng, X.B., Zhao, C.Z., Zhang, X.Q., Yan, C., Zhang, Q., and Huang, J.Q. (2019). Dual-phase single-ion pathway interfaces for robust lithium metal in working batteries. Adv. Mater. *31*, 1808392.

46. Onishi, K., Matsumoto, M., Nakacho, Y., and Shigehara, K. (1996). Synthesis of aluminate polymer complexes as single-ionic solid electrolytes. Chem. Mater. *8*, 469–472.

47. Fischer, S., Roeser, J., Lin, T.C., DeBlock, R.H., Lau, J., Dunn, B.S., Hoffmann, F., Fröba, M., Thomas, A., and Tolbert, S.H. (2018). A metal-organic framework with tetrahedral aluminate sites as a single-ion Li+ solid electrolyte. Angew. Chem. Int. Ed. *57*, 16683–16687.

48. Song, J., Ye, Q., Lee, W.T., Wang, X., He, T., Shah, K.W., and Xu, J. (2015). Perfluoropolyether/poly(ethylene glycol) triblock copolymers with controllable self-assembly behaviour for highly efficient anti-bacterial materials. RSC Adv. *5*, 64170–64179.

49. Park, S.K., Lee, J.M., Park, S., Kim, J.T., Kim, M.S., Lee, M.H., and Ju, J.J. (2011). Highly fluorinated and photocrosslinkable liquid prepolymers for flexible optical waveguides. J. Mater. Chem. *21*, 1755–1761.

50. Zheng, X., Zhang, Z., Tan, G., and Wang, X. (2016). An aliphatic solvent-soluble lithium salt of the Perhalogenated weakly coordinating anion [Al(OC(CCl 3)(CF 3) 2) 4] −. Inorg. Chem. *55*, 1008–1010.

51. Müller, L.O., and Krossing, I. (2008). A highly hexane soluble lithium salt and other starting materials of the fluorinated weakly coordinating anion [Al{OC(CF3)2(CH 2SiMe3)}4]-. Z. Anorg. Allg. Chem. *634*, 962–966.

52. Chen, H., Pei, A., Lin, D., Xie, J., Yang, A., Xu, J., Lin, K., Wang, J., Wang, H., Shi, F., et al. (2019). Uniform high ionic conducting lithium sulfide protection layer for stable lithium metal anode. Adv. Energy Mater. *9*, 1900858.

53. Zugmann, S., Fleischmann, M., Amereller, M., Gschwind, R.M., Wiemhöfer, H.D., and Gores, H.J. (2011). Measurement of transference numbers for lithium ion electrolytes via four different methods, a comparative study. Electrochim. Acta *56*, 3926–3933.

54. Yu, L., Chen, S., Lee, H., Zhang, L., Engelhard, M.H., Li, Q., Jiao, S., Liu, J., Xu, W., and Zhang, J.-G. (2018). A localized high-concentration electrolyte with optimized solvents and lithium difluoro(oxalate)borate additive for stable lithium metal batteries. ACS Energy Lett. *3*, 2059–2067.

55. Gao, Y., Yan, Z., Gray, J.L., He, X., Wang, D., Chen, T., Huang, Q., Li, Y.C., Wang, H., Kim, S.H., et al. (2019). Polymer–inorganic solid–electrolyte interphase for stable lithium metal batteries under lean electrolyte conditions. Nat. Mater. *18*, 384–389.

56. Choudhury, S., and Archer, L.A. (2016). Lithium fluoride additives for stable cycling of lithium batteries at high current densities. Adv. Electron. Mater. *2*, 1500246.

57. Xie, J., Wang, J., Lee, H.R., Yan, K., Li, Y., Shi, F., Huang, W., Pei, A., Chen, G., Subbaraman, R., et al. (2018). Engineering stable interfaces for three-dimensional lithium metal anodes. Sci. Adv. *4*, eaat5168.